Comparative Study of Linear Variable Flux Reluctance Machine with Linear Wound Field Flux Reversal Machine

Tingting Jiang, Liang Xu, *Member, IEEE*, Jinghua Ji, and Wenxiang Zhao, *Senior Member, IEEE*

***Abstract*—As members of doubly salient magnetless linear machines, linear variable flux reluctance (LVFR) and wound field flux reversal (LWFFR) machines inherit the merits of conventional magnetless linear machines such as low cost, high flux adjustment capability and high reliability. Furthermore, like linear switched reluctance machine, they have a very simple and compact long secondary, which are very attractive for long stroke applications. However, low force capability is their major defect. To solve this issue, new LVFR and LWFFR machine topologies were proposed in recent work, while lacking studies on their force improvement mechanism and further force evaluation. In this paper, LVFR and LWFFR machines with improved force performance are comparatively studied with the emphasis on their force capabilities. The operation principle of the two machines is analyzed based on magnetic field harmonics produced by flux modulation. Contributions of air-gap flux density harmonic components to no-load back electromagnetic forces of the two machines are analyzed and the average force equation is derived. Moreover, force capabilities of the both machines are investigated by means of the time-stepping finite-element analysis to verify the theoretical analysis.**

***Index Terms*—Wound field, Variable flux reluctance, Flux reversal, Linear machine, Finite-element analysis.**

I. INTRODUCTION

As the core power unit of actuator, machine is widely used in various field [1]-[3]. According to the transmission way, the machine can be divided into rotary machine [4], [5] and linear machine [6], [7]. Linear machines can directly serve in linear movement applications without the intermediate device to convert rotational movement to linear movement. Owing to the elimination of the intermediate device, the linear machines offer the advantages of simpler system structure and improved reliability, which have been widely applied in a lot of fields such as manufacturing industry, rail transportation and electromagnetic launch [8]-[17].

According to the case that whether permanent magnet (PM) material is employed, linear machines can be classified as PM linear machine and magnetless linear machine [18], [19]. Owing to the introduction of PMs, the PM linear machine has high force density and efficiency, while it suffers from the difficulty in flux adjustment and high cost of the PMs. Recently, in order to reduce the manufacturing cost and improve the flexibility of flux adjustment, there is a rapidly growing trend to develop the magnetless linear machines [16]-[22]. Conventional switched reluctance linear machines need not consume PMs, which can achieve the low cost and high flux adjustment capability, while suffering from relatively low force density. This is because that only inductance rising region in the full electrical period can be utilized to yield force. To improve the force performance and retain the merits of low manufacturing cost and simple secondary structure of the switched reluctance linear machine, various new kinds of magnetless doubly salient linear machines have been proposed. These new magnetless linear machines are characterized by the salient poles existed in the double sides, which is the same as the switched reluctance linear machine. Differing from the switched reluctance linear machine, the inductance in the full electrical period of these new magnetless linear machines can be utilized, which is conducive to improving force.

Linear wound field flux reversal (LWFFR) and linear variable flux reluctance (LVFR) machines are two typical machines, which belong to the new magnetless doubly salient linear machines. Recently, a few efforts were made to further improve their force capabilities. In [23], the LWFFR machines were designed based on magnetic gear effect. It manifested that with the consideration of the magnetic gear effect, force capability of the LWFFR machine is improved by about 37% as compared to conventional LWFFR machine. In [24], multi-tooth technique was employed in LVFR machine. It revealed that the multi-tooth LVFR machine can offer about 27% larger force than single-tooth LVFR machine. Actually, the proposed LWFFR and LVFR machines in [23], [24] exhibit very similar primary and secondary structures, i.e., multi-tooth in the primary and simple salient pole in the secondary. Also,

Manuscript received May 16, 2022; revised June 24, 2022; accepted July 18, 2022. Date of publication March 25, 2023; Date of current version January 11, 2023.

This work was supported in part by the National Natural Science Foundation of China under Grant 51977099 and Grant 52177044, in part by the Hong Kong Scholars Program under Grant XJ2019031, in part by the China Postdoctoral Science Foundation under Grant 2019T120395, in part by the Natural Science Foundation of Jiangsu Higher Education Institutions under Grant 21KJA470004, and in part by the Priority Academic Program Development of Jiangsu Higher Education Institutions. *(Corresponding author: Liang Xu.)*

The authors are with the School of Electrical and Information Engineering, the Jiangsu Key Laboratory of Drive and Intelligent Control for Electric Vehicle, and the National Center for International Research on Structural, Health Management of Critical Components, Jiangsu University, Zhenjiang 212013, China (e-mail: jtt@stmail.ujs.edu.cn; xuliang0511@ujs.edu.cn; jjh@ujs.edu.cn; zwx@ujs.edu.cn).

Digital Object Identifier 10.30941/CESTEMS.2023.00006

the difference is the location of field winding.

To date, the force improvements of the two machines have been confirmed by comparing their counterparts. However, there is a lack of studies on force improvement mechanism and further force evaluation of the two machines. The aim of this paper is to carry a comparison study of the two existing LVFR and LWFFR machines with the emphasis on the force capability. In Section II, operation principle of the two machines will be analyzed from the perspective of harmonics produced by flux modulation. Performance comparison will be conducted in Section III. Then, the parameter analysis of the superior LVFR machine is investigated in Section IV. Last, some conclusions will be given in Section V.

II. Analysis and Operation Principle

A. Topology

Fig. 1 depicts the topologies of the LWFFR and LVFR machines. As shown, the two machines share very similar topology features. Specifically, the PMs are removed in the two machines. The armature and field windings are all accommodated in their short primary, while they have simple and robust long secondary without PMs and windings. The armature and field windings are wound in a concentrated and non-overlapped manner, which is beneficial to reducing end length of windings and copper loss. The two machines have the same numbers of armature tooth and multi-tooth on the short primary, namely, 6 and 18 respectively. Apart from these similarities, there exist some differences in the two machines. The armature and field windings of the LVFR machine are both wound on the armature tooth, while that of the LWFFR one are wound on the armature tooth and multi-tooth, respectively. The connection of the windings is shown in Fig. 2. As can be seen, the armature winding of the two machines are wound in the same way, while the connections of field winding are different. Also, the salient pole numbers in the long secondary of the LWFFR and LVFR machines are 11 and 19, respectively. The design of different salient poles in the long secondary of the two machines is to achieve their optimal force performance.

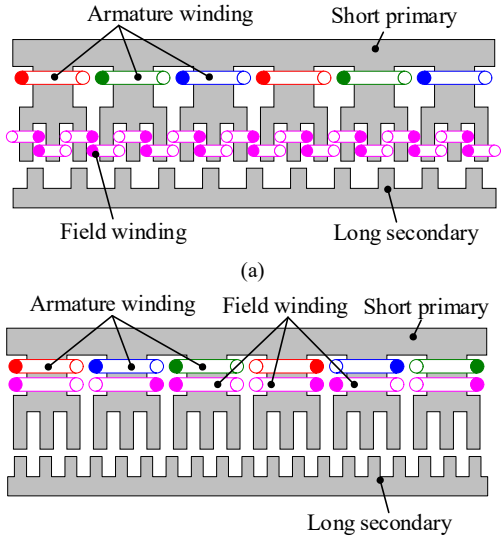

Fig. 1. Machine topologies. (a) LWFFR machine. (b) LVFR machine.

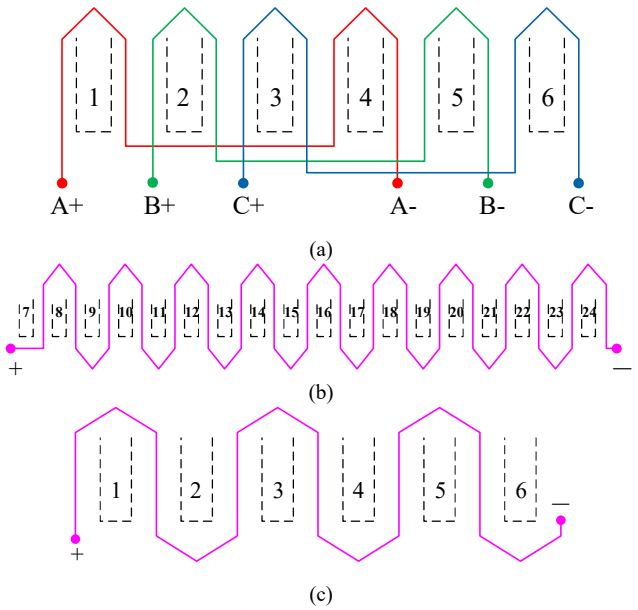

Fig. 2. Connection of the windings. (a) Armature winding of the two machines. (b) Field winding of LWFFR machine. (c) Field winding of LVFR machine.

B. Operation Principle

The two machines possess double side saliency due to the multi-tooth in the primary and salient pole in the secondary. With the flux modulation effect by the double side saliency, field winding magnetomotive force (MMF) can be modulated to produce plenty of air gap flux density harmonics. Fig. 3 shows the field winding MMF waveform of the two machines. Under the two successive armature teeth, the field winding MMF waveform of LWFFR machine forms three periods while of LVFR machine forms one period. The MMF excited by field winding can be written as

$$\begin{cases} F_1(\theta) = \sum_{i=1,3,5\ldots}^{\infty} F_i \sin(i\frac{3N_s}{2}\theta) \\ F_2(\theta) = \sum_{j=1,3,5\ldots}^{\infty} F_j \sin(j\frac{N_s}{2}\theta) \end{cases} \tag{1}$$

where $F_1(\theta)$ and $F_2(\theta)$ are the MMF of LWFFR and LVFR machines, respectively. F_i is the amplitude of the i^{th} MMF of LWFFR machine and F_j is the amplitude of the j^{th} MMF of LVFR machine. i and j are the odd number and N_s is the number of armature tooth. The F_i and F_j can be expressed as

$$\begin{cases} F_i = (-1)^{(i+3)/2}\frac{4N_f i_{dc}}{\pi i}\sin(i\frac{N_s\theta_{mt}}{4})[2\cos(i\frac{N_s\pi}{2})-1] \\ F_j = (-1)^{(j+3)/2}\frac{4N_f i_{dc}}{\pi j}\sin(j\frac{N_s\theta_{mt}}{4})[1+2\cos(j\frac{N_s\pi}{2})] \end{cases} \tag{2}$$

where N_f, i_{dc} and θ_{mt} are the number of field winding turns, the current of field winding and the arc of multi-tooth, respectively.

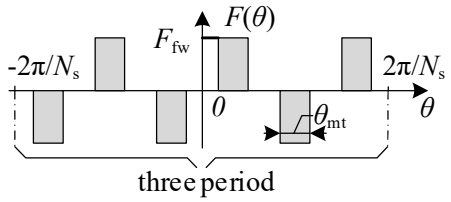

(a)

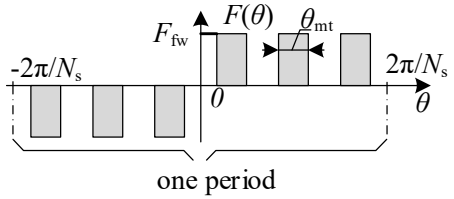

(b)

Fig. 3. MMF excited by field winding. (a) LWFFR machine. (b) LVFR machine.

Then, the permeance model about secondary salient pole is established, as shown in Fig. 4. Since the two machines have the same salient pole structure, their permeance model can be expressed as

$$P_r(\theta,t) = P_0 + \sum_{k=1,2,3\ldots}^{\infty} P_k \cos[kN_r(\theta - vt - \theta_0)] \tag{3}$$

where k is the positive integer, P_0 and P_k are the 0^{th} and j^{th} order harmonic component of secondary salient pole, respectively. θ_0 and v are the initial position and the velocity of the primary, respectively. P_0 and P_k can be written as

$$\begin{cases} P_0 = \dfrac{P_1 + P_2}{2} \\ P_k = \dfrac{P_1 - P_2}{k\pi} \sin(kN_r \dfrac{b_p}{2}) \end{cases} \tag{4}$$

where P_1 and P_2 are the maximum and minimum values of the permeance waveform, respectively. b_p is the secondary pole width.

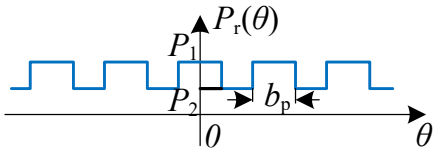

Fig. 4. Permeance of the salient pole in the secondary.

The flux density of two machines can be written as

$$\begin{cases} B_1(\theta,t) = F_1(\theta)P_r(\theta,t) = \sum_{i=1,3,5\ldots}^{\infty} F_i P_0 \sin(i\dfrac{3N_s}{2}\theta) \\ \quad + \dfrac{1}{2}\sum_{i=1,3,5\ldots}^{\infty}\sum_{k=1,2,3\ldots}^{\infty} F_i P_k \sin[(i\dfrac{3N_s}{2} \pm kN_r)\theta \mp kN_r(vt+\theta_0)] \\ B_2(\theta,t) = F_2(\theta)P_r(\theta,t) = \sum_{j=1,3,5\ldots}^{\infty} F_j P_0 \sin(j\dfrac{N_s}{2}\theta) \\ \quad + \dfrac{1}{2}\sum_{j=1,3,5\ldots}^{\infty}\sum_{k=1,2,3\ldots}^{\infty} F_j P_k \sin[(j\dfrac{N_s}{2} \pm kN_r)\theta \mp kN_r(vt+\theta_0)] \end{cases} \tag{5}$$

According to (5), the spatial order and the velocity of the corresponding harmonics of the two machines can be expressed as

$$\begin{cases} H_1(i,k) = 9i,\ v_1(i,k) = 0 \\ H_1(i,k) = 9i \pm 11k,\ v_1(i,k) = \dfrac{\pm 11kv}{9i \pm 11k} \end{cases} \tag{6}$$

$$\begin{cases} H_2(j,k) = 3j,\ v_2(j,k) = 0 \\ H_2(j,k) = 3j \pm 19k,\ v_2(j,k) = \dfrac{\pm 19kv}{3j \pm 19k} \end{cases} \tag{7}$$

The harmonics of the two machines are both divided into two groups by the harmonic velocity. The harmonics with $9i$ and $3j$ orders are stationary and the harmonics of $9i\pm11k$ and $3j\pm19k$ are rotary. Substituting the relevant parameters, Table I lists the main harmonics of the two machines. Although the two machines have the number of armature teeth, the period of field winding MMF and the salient pole of secondary are different. Therefore, the working harmonics have different orders.

TABLE I
MAIN HARMONICS OF TWO MACHINES

Group	Harmonic order									
	LWFFR					LVFR				
i/j	1	3	5	7	…	1	3	5	7	…
I	9	27	45	63	…	3	9	15	21	…
II	20	38	56	84	…	22	28	34	40	…
	2	6	34	52	…	16	10	4	2	…

Based on the winding theory [25]-[31], the virtual no-load phase back electromagnetic forces (back-EMFs) of the two machines can be derived as (8). The virtual no-load back-EMF is obtained when the field windings are excited with a direct current and the armature windings are open-circuited. The virtual no-load back-EMF is analogous to the no-load back-EMF produced by PMs in the PM machine.

$$e_a = 2vL_{stk}N_w \sin(vt)\sum_m \frac{N_r(-1)^{n_i}}{H_m} B_m k_{w(i)} \tag{8}$$

where L_{stk} and N_w are the stack length and armature winding turns per phase. H_m and B_m are the working flux density harmonic order and amplitude. n_i is used to distinguish the positive or negative contribution of the flux density harmonic to the no-load back-EMF. $k_{w(i)}$ represents the winding factor of the corresponding flux density harmonic.

Further, since their reluctance forces in the total average forces are negligible in the total average forces, d-axis zero current control is generally adopted for the two machines. Thus, their average forces can be given as:

$$F_{avg} = \frac{3EI}{v} = 3\sqrt{2}L_{stk}N_w I\sum_m \frac{N_r(-1)^{n_i}}{H_m} B_m k_{w(i)} \tag{9}$$

where E and I are the fundamental amplitude of virtual no-load phase back-EMF and phase armature current.

Fig. 5 illustrates the air-gap flux density waveforms of the two machines under only field winding excited. The analyzed machines have the same machine size. Also, the copper losses of field windings are kept the same as 60W, which correspond to 6414 ampere turn (A·t) for LWFFR and 6000 A·t for LVFR machines. As shown, in despite of relatively higher ampere turns applied in the LWFFR machine, its magnitude of air-gap flux density is only around ~ a third of that of the LVFR one. It is mainly resulted from the different field winding layouts, where the magnetic field modes on the multi-tooth in the short mover by the field windings are NSN-SNS-NSN and SSS-NNN-SSS for the LWFFR and LVFR machines, respectively.

Fig. 6 depicts the air-gap flux density harmonic spectra of the two machines under only field winding excited. According to the flux modulation principle, abundant air-gap flux density harmonics are generated in the two machines. It can be seen

that the results of finite-element analysis (FEA) are in agreement with the theoretical analysis.

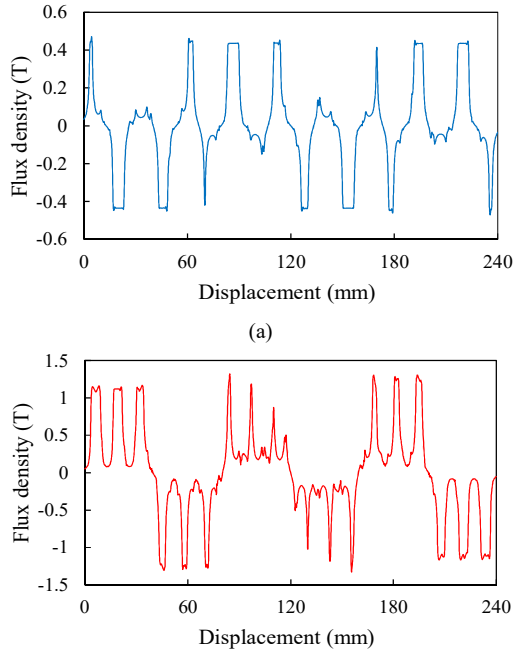

Fig. 5. Air-gap flux density waveforms of the two machines under only field winding excited. (a) LWFFR machine. (b) LVFR machine.

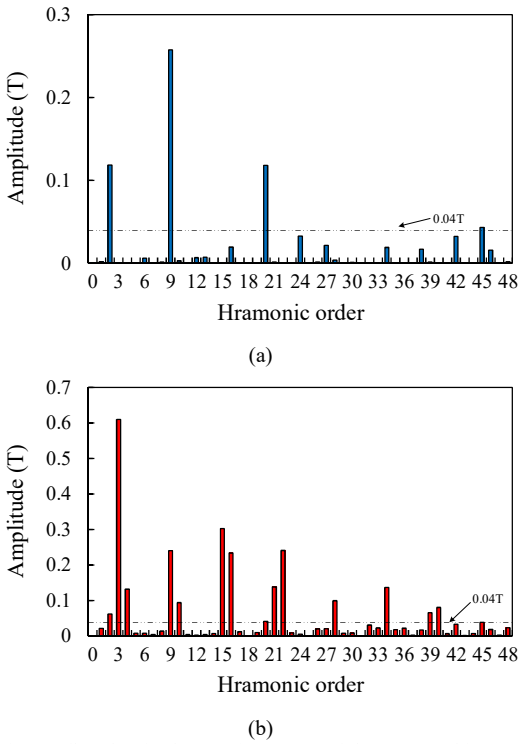

Fig. 6. Air-gap flux density harmonic spectra of the two machines under only field winding excited. (a) LWFFR machine. (b) LVFR machine.

Table II lists the fundamental back-EMFs by analytical method and FEA. Considering the fact that the low order harmonics dominate the contribution of back-EMF, only the working flux density harmonics with amplitude exceeding 0.04T and order not exceeding 35 are considered in analytical calculation to the fundamental back-EMFs of the two machines. As shown in Table II, the LVFR machine has more working flux density harmonics than the LWFFR one when only the working flux density harmonics with amplitude exceeding 0.04T and order not exceeding 35 are considered.

The working harmonics generating fundamental no-load back-EMF of the LWFFR machine are 2nd and 10th and that of the LVFR machine are 2nd, 4th, 10th, 16th, 20th, 22nd, 28th and 34th, as summarized in Table II. As shown, the LVFR machine has many more flux density harmonics to yield back-EMF than the LWFFR one. Also, the LVFR machine offers a significantly larger back-EMF than the LWFFR one. Besides, the analytical back-EMF results agree well with the FEA results, which verify the effectiveness of the theoretical analysis.

TABLE II
FUNDAMENTAL BACK-EMF PRODUCTION BY FLUX DENSITY HARMONICS OF THE TWO MACHINES

	LWFFR machine							
Harmonic order	2				20			
Back-EMF (V) (analytical results)	22.58				-2.25			
Back-EMF (%) (Analytical results)	111.1				-11.1			
Total back-EMF (V) (Analytical results)/ (FEA results)	20.3/21.5							
	LVFR machine							
Harmonic order	2	4	10	16	20	22	28	34
Back-EMF (V) (Analytical results)	20.37	21.68	6.18	9.61	1.35	-7.2	-2.33	-2.65
Back-EMF (%) (Analytical results)	39.2	41.7	11.9	18.5	2.6	-13.86	-4.49	-5.1
Total back-EMF (V) (Analytical results)/ (FEA results)	52.0/56.2							

III. PERFORMANCE COMPARISON

In order to obtain a fair comparison, the primary width, machine high, stack length and air gap length of the two machines are designed with the identical size. The genetic algorithm is adopted and coupled with FEA to maximize their average forces at the fixed total copper loss. Fig. 7 illustrates the key design parameters of the two machines. In the optimization algorithm, numbers of generations and individuals are set as 10 and 20, respectively. Optimization results are listed in Table III.

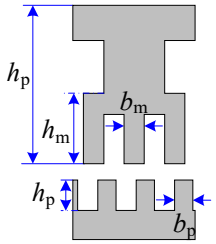

Fig. 7. Illustration of the key design parameters of the two machines.

TABLE III
SPECIFICATIONS OF THE TWO MACHINES

Item	LWFFR	LVFR
Primary width, b_{mp} (mm)	240	
Machine high, h_{mp} (mm)	80	
Stack length, L_{stk} (mm)	100	
Air gap length, δ (mm)	0.5	
Total copper loss, P_c (W)	120	
Number of armature winding turns, N_w	100	
Number of field winding turns, N_f	100	

Primary/secondary materials	Laminated silicon steel	
Primary high, h_p (mm)	56.4	56.6
Multi-tooth width, b_m (mm)	6.5	4.5
Multi-tooth high, h_m (mm)	17.9	5.4
Secondary pole width, b_p (mm)	8.6	4.5
Secondary pole high, h_p (mm)	7.8	6.9

A. No-Load Flux Density Distribution and back-EMF

Fig. 8 shows the flux density distributions of the two optimized machines under no-load condition in which only field windings are excited. It can be observed that the heights of the multi-tooth are distinct, in which the height of the multi-tooth of the LWFFR machine is much larger than that of the LVFR one so as to accommodate the field windings. Also, as shown, the LWFFR machine has more flux leakage between adjacent small teeth as compared to the LVFR machine.

Furthermore, no-load phase back-EMFs of the two optimized machines with the same number of armature winding turns are illustrated in Fig. 9. Both of them possess sinusoidal and symmetrical waveforms. Also, the fundamental components are dominant in the two machines while harmonic components are negligible. Much larger fundamental back-EMF is achieved in the LVFR machine, which coincides with the aforementioned operation principle analysis.

And, the fundamental back-EMF with different copper loss is plotted in Fig. 10. The copper loss is only the loss of field winding current under the no-load condition. It can be seen that the fundamental back-EMFs increases and then decrease as the copper loss increases for the LVFR machine. The fundamental back-EMF reaches the maximum at the copper loss is 60W. For the LWFFR machine, the fundamental back-EMF increases as the copper loss increase. The fundamental back-EMFs of LVFR machine are obviously higher than that of LWFFR machine.

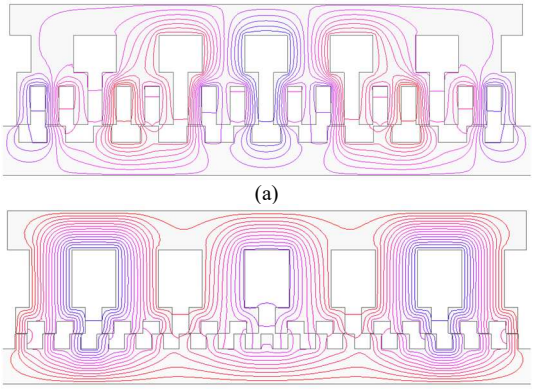

(a)

(b)

Fig. 8. Flux density distributions of the two machines under no-load condition. (a) LWFFR machine. (b) LVFR machine.

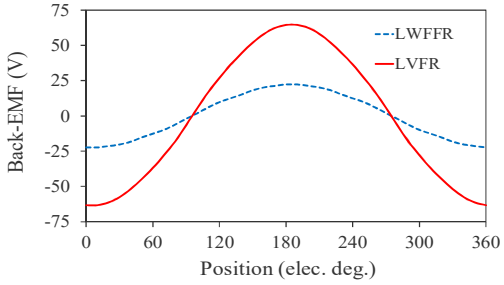

(a)

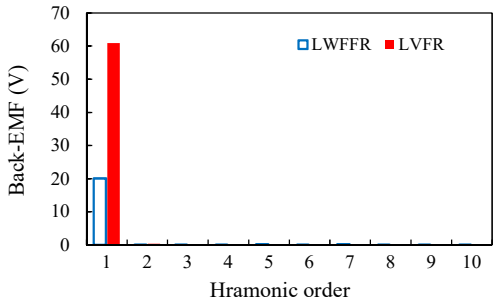

(b)

Fig. 9. No-load phase back-EMFs of the two machines. (a) Waveforms. (b) Spectra.

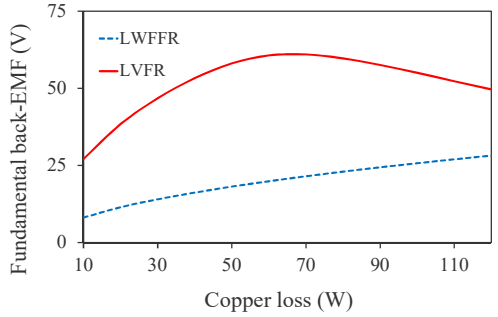

Fig. 10. No-load phase fundamental back-EMFs with different copper losses.

B. On-Load Force and Magnetic Flux Density

Under the on-load condition of armature winding copper loss is 60W and field winding copper loss is 60W. Fig. 11 shows their force results of the two machines. As can be seen, the LVFR machine has the merit of the enhanced average force as compared to the LWFFR one. Also, both the machines suffer from relatively large force ripples. It can be calculated that the average forces of the LWFFR and LVFR machines are 149.4 N and 362.5 N, respectively, while their ripple coefficients are 17.3 % and 15.7 %, respectively. The LVFR machine offers a 142% higher average force than the LWFFR one. Furthermore, the magnetic flux density of the two machines is plotted in Fig. 12. The maximum magnetic flux density area of LWFFR and LVFR machines are in the multi-tooth and armature tooth, respectively. Then, the force with the different armature winding current angle of two machines is investigated in Fig. 13. For the LWFFR machine, the force decreases with the increase of current angle. The force rises slightly and then decreases with the increase of current angle in the LVFR machine.

In Fig. 14, under total copper loss is 120W, ratio of the armature winding copper loss to the total copper loss on the force capability of the two machines is analyzed. As depicted, the LVFR machine offers the enhanced force capability under the same distribution ratio of copper loss in the whole region. Also, the forces of the two machines increase with the ratio of the armature winding copper loss to the total loss then reduce. It reveals that both the machines achieve their maximum forces when the distribution ratio of copper loss is 0.4.

IV. KEY PARAMETER ANALYSIS OF THE LVFR MACHINE

By the above comparison of the two machines, it can be

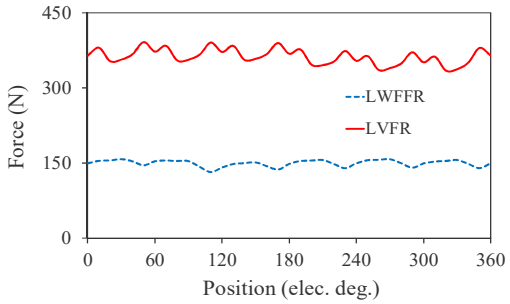

Fig. 11. Electromagnetic force of the two machines.

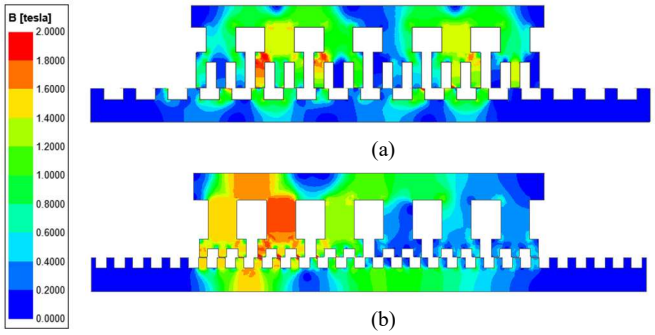

Fig. 12. Magnetic flux density of the two machines under on-load condition. (a) LWFFR machine. (b) LVFR machine.

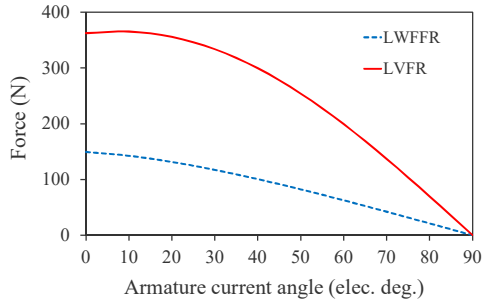

Fig. 13. Electromagnetic force variation with armature current angle.

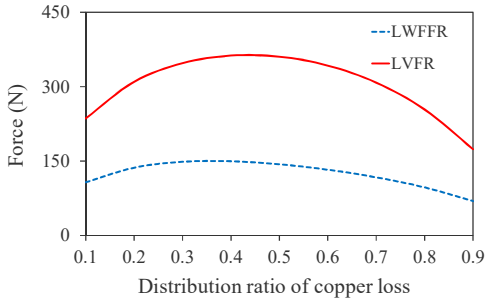

Fig. 14. Electromagnetic force variation with ratio of armature winding copper loss to total copper loss of the two machines.

found that the LVFR machine has better force capacity with the same copper loss. Then, the superior LVFR machine is selected to further investigate.

The force variation with multi-tooth width b_m and secondary pole width b_p are plotted in Figs 15 and 16, respectively. It can be seen that the force increases first and then decreases with the increase of b_m and b_p. And, according to the variation range of the force, the two parameters have a great influence on the force. The optimal values of b_m and b_p are both 4.5mm.

Fig. 17 shows the influence of copper loss on force. In the condition of different copper loss, the ratio of armature winding copper loss to the total loss is 0.4. It can be seen that the force increases with increase of the copper loss. Due to the influence of saturation, the force appreciation is obviously slow when the copper loss exceeds 140W.

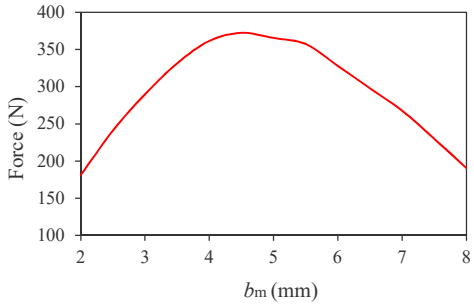

Fig. 15. Electromagnetic force variation with multi-tooth width b_m.

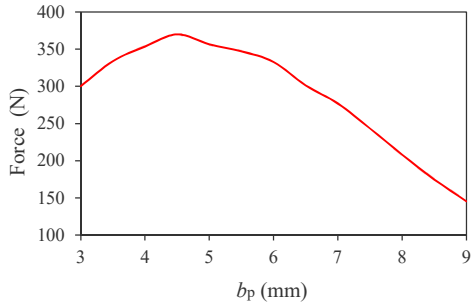

Fig. 16. Electromagnetic force variation with secondary pole width b_p.

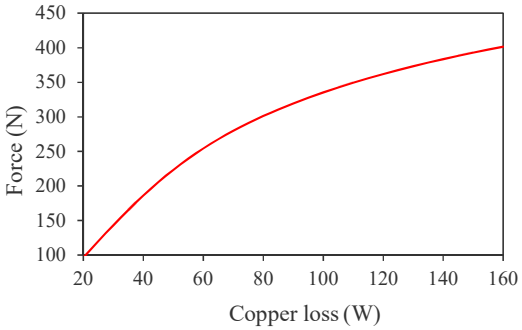

Fig. 17. Electromagnetic force variation with copper loss.

V. Conclusion

In this paper, two typical doubly salient magnetless linear machines, namely, the LWFFR and LVFR machines have been comparatively investigated with the emphasis on the force capability. The operation principle of the two machines was analyzed from the perspective of the harmonics produced by flux modulation. The harmonic contribution to fundamental no-load back-EMF was derived and calculated. It was shown that more harmonics in the LVFR machines engage to produce force. So, significantly enhanced force capability is achieved in the LVFR machine. The FEA results proved that the force capability of the LVFR machine is superior to the LWFFR one under the same condition. Hence, the LVFR machine is more suitable for some applications which need a high force. And, the influence of key parameters on force is analyzed about LVFR machine.

References

[1] X. Li, Z. Xue, X. Yan, L. Zhang, W. Ma, and W. Hua. “Low-complexity

multivector-based model predictive torque control for PMSM with voltage preselection". *IEEE Trans. Power Electron*., vol. 36, no. 10, pp. 11726-11738, Oct. 2021.

[2] X. Li, Z. Xue, L. Zhang, and W. Hua. "A low-complexity three-vector-based model predictive torque control for SPMSM". *IEEE Trans. Power Electron*., vol. 36, no. 11, pp. 13002-13012, Nov. 2021.

[3] X. Sun, J. Cao, G. Lei, Y. Guo, and J. Zhu, "Speed sensorless control for permanent magnet synchronous motors based on finite position set," *IEEE Trans. Ind. Electron*., vol. 67, no. 7, pp. 6089-6100, Jul. 2020.

[4] B. Wang, J. Wang, A. Griffo, and B. Sen, "A general modeling technique for a triple redundant 3×3-phase PMA SynRM," *IEEE Trans. Ind. Electron*., vol. 65, no. 11, pp. 9068-9078, Nov. 2018.

[5] B. Wang, J. Hu, W. Hua, M. Cheng, G. Wang and W. Fu, "Multiple 3-phase PMA-SynRM with delta windings for enhanced fault tolerance," *IEEE Trans. Ind. Electron*., doi: 10.1109/TIE.2022.3156146.

[6] J. Ge, W. Xu, Y. Liu, F. Xiong and D. Li, "Investigation on winding theory for short primary linear machines," *IEEE Trans. Veh. Tech.*, vol. 70, no. 8, pp. 7400-7412, Aug. 2021.

[7] X. Li, W. Xu, K. Liao and X. Wu, "Design of stator-magnet moving-iron transverse-flux linear oscillatory machine considering asymmetric saturation," *IEEE Trans. Transport. Electrific*., doi: 10.1109/TTE.2022.3152909.

[8] G. Lv, T. Zhou, D. Zeng, and Z. Liu, "Design of ladder-slit secondaries and performance improvement of linear induction motors for urban rail transit," *IEEE Trans. Ind. Electron*., vol. 65, no. 2, pp. 1187-1195, Feb. 2018.

[9] W. Zhao, T. Yao, L. Xu, X. Chen and X. Song, "Multi-objective optimization design of a modular linear permanent-magnet vernier machine by combined approximation models and differential evolution," *IEEE Trans. Ind. Electron.*, vol. 68, no. 6, pp. 4634-4645, June 2021.

[10] F. Bian, W. Zhao, J. Ji, L. Xu, H. Chen and M. Gao, "Mechanism investigation of ring type winding in linear permanent magnet vernier machine for improving force density," *IEEE Trans. Veh. Technol*., vol. 69, no. 3, pp. 2588-2597, March 2020.

[11] R. Cao, M. Lu, N. Jiang and M. Cheng, "Comparison between linear induction motor and linear flux-switching permanent-magnet motor for railway transportation," *IEEE Trans. Ind. Electron*., vol. 66, no. 12, pp. 9394-9405, Dec. 2019,

[12] M. Yuan and S. Niu, "Design and analysis of a novel modular linear double-stator biased flux machine," *IEEE Trans. Magn*., vol. 54, no. 11, Art no. 8108905, Nov. 2018.

[13] H. Chen, R. Nie and W. Yan, "A novel structure single-phase tubular switched reluctance linear motor," *IEEE Trans. Magn*., vol. 53, no. 11, Art no. 8205804, Nov. 2017.

[14] J. Luo, B. Kou, H. Zhang and R. Qu, "Development of a consequent pole transverse flux permanent magnet linear machine with passive secondary structure," *CES Trans. Electr. Mach. Syst*., vol. 3, no. 1, pp. 39-44, March 2019.

[15] Q. F. Lu and W. H. Mei, "Recent development of linear machine topologies and applications," *CES Trans. Electr. Mach. Syst*., vol. 2, no. 1, pp. 65-72, March 2018.

[16] D. Wang, X. Wang and X. Du, "Design and comparison of a high force density dual-side linear switched reluctance motor for long rail propulsion application with low cost," *IEEE Trans. Magn.*, vol. 53, no. 6, Art no. 7207204, Jun. 2017.

[17] Z. Zeng and Q. Lu, "A novel hybrid-excitation switched-flux linear machine with partitioned-excitations," *IEEE Trans. Magn.*, vol. 55, no. 12, Art no. 7502204, Dec. 2019.

[18] C. H. T. Lee, K. T. Chau, C. Liu and C. C. Chan, "Overview of magnetless brushless machines," *IET Electr. Power Appl*., vol. 12, no. 8, pp. 1117-1125, Aug. 2018.

[19] T. W. Ching, Y. Shi, W. Li and L. Jian, "Design and analysis of a magnetless linear variable reluctance motor with modular mover units for electric propulsion," *IEEE Trans. Appl. Supercond*., vol. 30, no. 4, pp. 1-5, June 2020.

[20] I. Boldea, L. N. Tutelea, L. Parsa, and D. G. Dorrell, "Automotive electric propulsion systems with reduced or no permanent magnets: an overview," *IEEE Trans. Ind. Electron*., vol. 61, no. 10, pp. 5696-5711, Oct. 2014.

[21] Y. Wang, W. Xu, X. Zhang and W. Ma, "Harmonic analysis of air gap magnetic field in flux-modulation double-stator electrical-excitation synchronous machine," *IEEE Trans. Ind. Electron*., vol. 67, no. 7, pp. 5302-5312, Jul. 2020.

[22] X. Li, X. Wang, and S. Yu, "Design and analysis of a novel transverse-flux tubular linear switched reluctance machine for minimizing force ripple," *IEEE Trans. Transport. Electrific*., vol. 7, no. 2, pp. 741-753, Jun. 2021.

[23] L. Xu, G. Liu, W. Zhao, J. Ji, H. Zhou and T. Jiang, "Design and analysis of a new linear wound-field flux reversal machine based on magnetic gear effect," *IEEE Trans. Magn*., vol. 51, no. 11, Art no. 8205004, Nov. 2015.

[24] Y. Shen and Q. Lu, "Investigation of novel multi-tooth linear variable flux reluctance machines," *IEEE Trans. Magn.*, vol. 54, no. 11, Art no. 8107905, Nov. 2018.

[25] M. Cheng, P. Han, and W. Hua, "General airgap field modulation theory for electrical machines," *IEEE Trans. Ind. Electron.*, vol. 64, no. 8, pp. 6063-6074, Aug. 2017.

[26] T. Zou, D. Li, R. Qu, D. Jiang and J. Li, "Advanced high torque density pm vernier machine with multi working harmonic," *IEEE Trans. Ind. Appl*., vol. 53, no. 6, pp. 5295-5304, Nov. 2017.

[27] Z. Wu and Z. Q. Zhu, "Analysis of air-gap field modulation and magnetic gearing effects in switched flux permanent magnet machines," *IEEE Trans. Magn*., vol. 51, no. 5, 8105012, May 2015.

[28] Q. Wang and S. Niu, "Design, modeling, and control of a novel hybrid-excited flux-bidirectional-modulated generator-based wind power generation system," *IEEE Trans. Power Electron*., vol. 33, no. 4, pp. 3086-3096, Apr. 2018.

[29] L. Xu, W. Wu, and W. Zhao, "Airgap magnetic field harmonic synergetic optimization approach for power factor improvement of PM vernier machines," *IEEE Trans. Ind. Electron*., doi: 10.1109/TIE.2021.3135634.

[30] T. Jiang, W. Zhao, L. Xu, and J. Ji, "A novel parallel hybrid excitation field modulated machine with efficient utilization of multi-working harmonics," *IEEE Trans. Ind. Electron*., vol. 69, no. 2, pp. 1177-1188, Feb. 2022.

[31] L. Xu, W. Zhao, R. Li, and S. Niu, "Analysis of rotor losses in permanent magnet vernier machines," *IEEE Trans. Ind. Electron.*, vol. 69, no. 2, pp. 1224-1234, Feb. 2022.

Tingting Jiang received the M.S. degree in electrical engineering from Jiangsu University, Zhenjiang, China, in 2015. She is currently working toward the Ph.D. degree in electrical engineering with Jiangsu University, Zhejiang, China. Her research interests include machine design and electromagnetic field analysis.

Liang Xu (Member, IEEE) received the B.Sc. degree in electrical engineering and automation from Soochow University, Suzhou, China, in 2011, the M.Sc degree in power electronics and power drives from Jiangsu University, Zhenjiang, China, in 2014, and the Ph.D. degree in control science and engineering from Jiangsu University, Zhenjiang, China, in 2017.

Since 2017, he has been with Jiangsu University, where he is currently an Associate Professor in the School of Electrical Information Engineering. Since 2021, he serves as a Postdoctoral Fellow with the department of Electrical Engineering, The Hong Kong Polytechnic University under Hong Kong Scholars Program. His areas of interest include electrical machines and drives.

Jinghua Ji received the B.Sc., M.Sc., and Ph.D. degrees in electrical engineering from Jiangsu University, Zhenjiang, China, in 2000, 2003, and 2009, respectively.

Since 2000, she has been with the School of Electrical and Information Engineering, Jiangsu University, where she is currently a Professor. From 2013 to 2014, she was a Visiting Scholar with the Department of Electronic and Electrical Engineering, University of Sheffield, Sheffield, U.K. She has authored or coauthored over 50 technical papers in these areas. Her research interests include electrical machines and motor drives.

Wenxiang Zhao (Senior Member, IEEE) received the B.Sc. and M.Sc. degrees in electrical engineering from Jiangsu University, Zhenjiang, China, in 1999 and 2003, respectively, and the Ph.D. degree in electrical engineering from Southeast University, Nanjing, China, in 2010.

He has been with Jiangsu University since 2003, where he is currently a Professor with the School of Electrical Information Engineering. From 2008 to 2009, he was a Research Assistant with the Department of Electrical and Electronic Engineering, University of Hong Kong, Hong Kong. From 2013 to 2014, he was a Visiting Professor with the Department of Electronic and Electrical Engineering, University of Sheffield, Sheffield, U.K. He has authored and coauthored over 150 papers published in various IEEE TRANSACTIONS. His current research interests include electric machine design, modeling, fault analysis, and intelligent control.